

Crystallinity Regulated Functional Separator Based on Bimetallic Ni_xFe_y Alloy Nanoparticles for Facilitated Redox Kinetics of Lithium–Sulfur Batteries

Qing Liu, Xiaotong Han, Zhiyong Zheng, Peixun Xiong, Rag-Gyo Jeong, Gildong Kim, Hyunyoung Park, Jongsoon Kim,* Bo-Kyong Kim,* and Ho Seok Park*

The practical application of lithium–sulfur batteries (LSBs) is limited by the shuttle effect of lithium polysulfides (LiPSs), large volume expansion, and sluggish conversion kinetics of sulfur. Herein, the crystallinity regulation of Ni_xFe_y alloy anchored on oxidized carbon nanotube/nitrogen-doped graphene (Ni_xFe_y@OCNT/NG) for application of a functional separator into LSBs is demonstrated. A low crystalline Ni_xFe_y@OCNT/NG (LC-Ni_xFe_y@OCNT/NG) modified polypropylene separator is systematically compared with its highly crystalline counterpart (HC-Ni_xFe_y@OCNT/NG), demonstrating superior LiPS absorbability, redox mediating capability into facilitated conversion kinetics, and uniform flux of Li⁺ into the anode. Furthermore, theoretical calculations confirm that the LC-Ni_xFe_y alloy features high adsorption energies and low diffusion energy barriers toward LiPSs, as well as a decreased energy gap and larger electron density near Fermi level. Accordingly, the LSB cells with LC-Ni_xFe_y@OCNT/NG modified separators deliver a high specific capacity of 1379.13 mA h g⁻¹ at 0.1 C and a low decay ratio of 0.04%/cycle over 600 cycles at 5.0 C with a high capacity of 410 mA h g⁻¹. Even under high sulfur loading (5.37 mg cm⁻²) and lean electrolyte (E/S = 4.9 μL mg⁻¹) conditions, the LSB cells with LC-Ni_xFe_y@OCNT/NG/PP deliver a high areal capacity of 4.1 mAh cm⁻² at 0.2 C.

advanced energy storage devices with large energy densities and low cost is rapidly increasing to replace the existing lithium-ion batteries. In particular, lithium–sulfur batteries (LSBs) are regarded as a promising candidate owing to their high energy density (≈2600 Wh kg⁻¹) and low cost of sulfur active materials.^[1,2] However, the practical application of LSBs is seriously impeded by several obstacles, such as the shuttle effect derived from the dissolution and diffusion of lithium polysulfides (LiPSs), drastic volume expansion/contraction during repeated cycles, and low electrical conductivity of sulfur, which are attributed to low sulfur utilization, rapid capacity decay, and sluggish redox kinetics.^[3,4] Various chemical strategies including the design of sulfur host materials,^[5–9] electrolyte,^[10] and functional interlayers/separators^[11,12] have been developed to resolve the above issues. In particular, the separator modification is beneficial for suppressing LiPSs migration and for mitigating the shuttle effect

while not reducing the sulfur contents for the large energy density of full cells.^[13,14] Materials for separator modification include conductive carbon materials, inorganic compounds, and hybrid materials.^[15–19] However, these are still limited by

1. Introduction

Motivated by the continuous development of portable electronic devices and electrical vehicles, the strong demand for

Q. Liu, X. Han, P. Xiong, H. S. Park
School of Chemical Engineering
Sungkyunkwan University
2066, Seoburo, Jangan-gu, Suwon 440-746, Republic of Korea
E-mail: phs0727@skku.edu

Q. Liu, R.-G. Jeong, G. Kim, B.-K. Kim
Smart Electrical & Signaling Division
Korea Railroad Research Institute (KRRRI)
176, Cheoldobangmulgan-ro, Uiwang-si 16105, Republic of Korea
E-mail: bkkim@krrri.re.kr

X. Han
College of Chemistry and Chemical Engineering
Chongqing University
Chongqing 400044, P. R. China

 The ORCID identification number(s) for the author(s) of this article can be found under <https://doi.org/10.1002/adfm.202207094>.

Z. Zheng
Department of Chemistry
Sungkyunkwan University
2066, Seoburo, Jangan-gu, Suwon 440-746, Republic of Korea

H. Park, J. Kim
Department of Energy Science
Sungkyunkwan University
2066, Seobu-ro, Jangan-gu
Suwon, Gyeonggi-do 440-746, Republic of Korea
E-mail: jongsoonkim@skku.edu

H. Park, J. Kim, H. S. Park
SKKU Institute of Energy Science and Technology (SIEST)
Sungkyunkwan University
2066, Seobu-ro, Jangan-gu
Suwon, Gyeonggi-do 440-746, Republic of Korea

DOI: 10.1002/adfm.202207094

limited LiPS absorbability, suppressed Li^+ transportation, and low sulfur utilization efficiency.

Transition metal-based alloys are considered a promising host material of sulfur active materials owing to their high electrochemical conductivity and electrocatalytic activity.^[20,21] Among them, bimetallic alloys (FeNi , FeCo , Co_7Fe_3 , and Co_xSn_y) are featured with their strong adsorption capability and excellent electrocatalytic activity toward LiPSs conversion.^[22–25] Despite these benefits of bimetallic alloy-based sulfur hosts, their separator modifications for LSBs have been rarely reported. Taking consideration into the surface conversion reaction of LiPSs, the abundant active sites and large accessible surface areas of the bimetallic alloys need to be achieved. In sharp contrast to the highly crystalline nanomaterials, the low crystalline or amorphous nanomaterials are featured with relatively unsaturated electronic configurations, numerous randomly oriented bonds, and abundant defect sites, which benefit to obtain an efficient LiPSs catalyst via the regulation of crystallinity.^[26–28] Thus, the crystallinity effect of bimetallic alloys on the surface adsorption and redox kinetics of LiPSs conversion should be explored for the rational design of functional separators.^[28]

Herein, we have demonstrated the high and low crystalline Ni_xFe_y alloy anchored on oxidized carbon nanotube/nitrogen-doped graphene (HC- and LC- $\text{Ni}_x\text{Fe}_y@OCNT/NG$) for the modification of polypropylene (PP) separators. The abundant active sites of the LC- $\text{Ni}_x\text{Fe}_y@OCNT/NG$ on the large accessible area are attributed to strong chemisorption capability toward LiPSs and facilitated conversion kinetics as confirmed by experimental results and density functional theory (DFT) calculations. Combining the redox mediating capability of LC- Ni_xFe_y alloy with the 3D conductive network of OCNT/NG, the LSBs with the LC- $\text{Ni}_x\text{Fe}_y@OCNT/NG$ modified separators achieved a high specific capacity, excellent rate performance, and long cyclic stability even with a high sulfur loading of 5.37 mg cm^{-2} and a lean electrolyte of $E/S = 4.9 \mu\text{L mg}^{-1}$. This work highlights the

importance of regulating the crystallinity of bimetallic alloys for the design of functional separators into highly efficient LSBs.

2. Results and Discussion

The LC- $\text{Ni}_x\text{Fe}_y@OCNT/NG$ and HC- $\text{Ni}_x\text{Fe}_y@OCNT/NG$ were synthesized by adjusting the amounts of two precursors such as $\text{Fe}(\text{NO}_3)_3 \cdot 9\text{H}_2\text{O}$ and $\text{Ni}(\text{NO}_3)_2 \cdot 6\text{H}_2\text{O}$ (Figures S1 and S2, Supporting Information). In the pyrolysis process under N_2 atmosphere, the Ni^{2+} and Fe^{3+} species were converted to Ni_xFe_y alloys with OCNT and NG. The morphology of the LC- $\text{Ni}_x\text{Fe}_y@OCNT/NG$ and HC- $\text{Ni}_x\text{Fe}_y@OCNT/NG$ were investigated using scanning electron microscopy (SEM) and transmission electron microscopy (TEM). Both the LC- $\text{Ni}_x\text{Fe}_y@OCNT/NG$ and HC- $\text{Ni}_x\text{Fe}_y@OCNT/NG$ feature a uniform distribution of Ni_xFe_y alloy nanoparticles on the 3D open porous channels of conductive OCNT/NG supporters (Figures S3 and S4, Supporting Information). TEM images show that most of Ni_xFe_y alloy nanoparticles with the size of 5–15 nm are tightly combined with OCNT/NG skeleton, which is consistent with the SEM images (Figures S5 and S6, Supporting Information). The energy-dispersive X-ray (EDX) mapping images present that both Ni and Fe elements are uniformly distributed in the selected area, indicating the alloying of Ni and Fe (Figures S7 and S8, Supporting Information).

As shown in the high-resolution TEM (HR-TEM) image of LC- $\text{Ni}_x\text{Fe}_y@OCNT/NG$ (Figure 1A), the Ni_xFe_y nanoparticles are tightly deposited onto the OCNT and NG surfaces. The absence of lattice fringes is attributed to the low crystalline nature of Ni_xFe_y alloy, as confirmed by the enlarged HR-TEM image and selected area electron diffraction (SAED) pattern (Figure 1C). The HC- $\text{Ni}_x\text{Fe}_y@OCNT/NG$ shows a similar structure to LC- $\text{Ni}_x\text{Fe}_y@OCNT/NG$ (Figure 1B), but the well-indexed lattice fringes of the former indicate the highly crystalline nature of

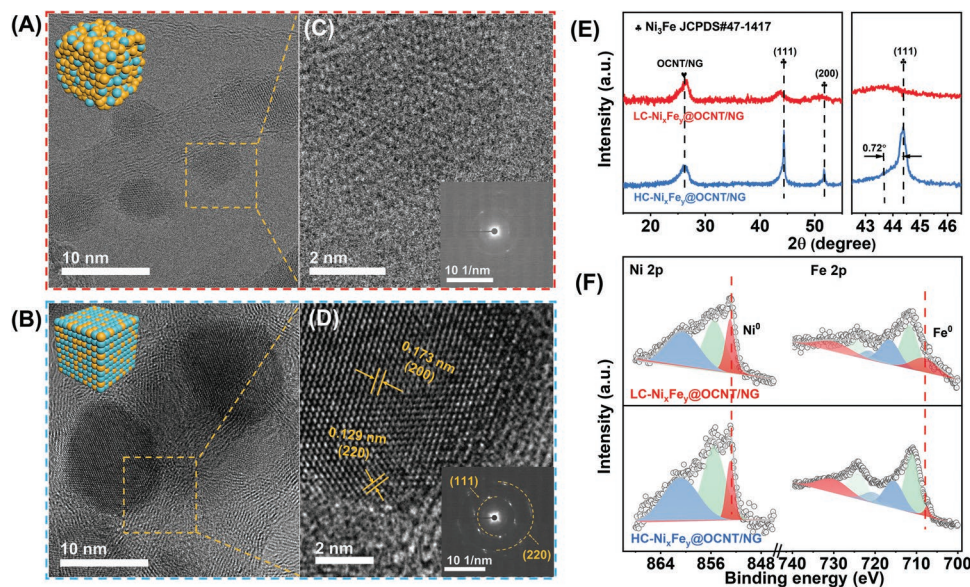


Figure 1. A,B) TEM, C,D) HRTEM images and SAED patterns, E,F) XRD patterns and Ni 2p, Fe 2p spectra of HC- $\text{Ni}_x\text{Fe}_y@OCNT/NG$ and LC- $\text{Ni}_x\text{Fe}_y@OCNT/NG$ nanocomposites.

Ni_xFe_y alloy. Specifically, the lattice fringes with d -spacings of 0.173 and 0.129 nm are indexed to the (200) and (220) planes of Ni_xFe_y alloy, and the distinct diffraction rings of SAED pattern correspond to (111) and (220) planes (Figure 1D). The proportions of Ni and Fe for LC- $\text{Ni}_x\text{Fe}_y@$ OCNT/NG and HC- $\text{Ni}_x\text{Fe}_y@$ OCNT/NG were quantitatively determined by inductively coupled plasma-optical emission spectrometry (ICP-OES). The Ni/Fe ratios of LC- $\text{Ni}_x\text{Fe}_y@$ OCNT/NG and HC- $\text{Ni}_x\text{Fe}_y@$ OCNT/NG are 0.35 and 3.19, respectively, in good agreement with their stoichiometric ratios (Table S1, Supporting Information). These results indicate that the large content of Fe plays an important role in the formation of low crystalline Ni_xFe_y alloy for LC- $\text{Ni}_x\text{Fe}_y@$ OCNT/NG.

The crystalline structures of LC- $\text{Ni}_x\text{Fe}_y@$ OCNT/NG and HC- $\text{Ni}_x\text{Fe}_y@$ OCNT/NG were characterized using X-ray diffraction (XRD) spectroscopy. As shown in Figure 1E, the HC- $\text{Ni}_x\text{Fe}_y@$ OCNT/NG shows two sharp diffraction peaks at 44.3° and 51.7° , respectively, corresponding to the (111) and (200) crystal planes of Ni_xFe_y alloy (PDF # 47–1417), which confirms the highly crystalline nature of Ni_xFe_y alloy. By contrast, two weak peaks of Ni_xFe_y alloy were observed for the LC- $\text{Ni}_x\text{Fe}_y@$ OCNT/NG, verifying its low crystalline nature. Moreover, the diffraction peak of (111) plane for LC- $\text{Ni}_x\text{Fe}_y@$ OCNT/NG shows a down-shift by $\approx 0.72^\circ$, which indicates the lattice distortion with enlarged lattice distance by a large Fe content in Ni_xFe_y alloy. The distinct peak at 26° for both samples is assigned to the (002) crystal plane of OCNT and NG. Furthermore, the similar intensity ratios of D- and G-band (I_D/I_G) in Raman spectra elucidate that both LC- $\text{Ni}_x\text{Fe}_y@$ OCNT/NG and HC- $\text{Ni}_x\text{Fe}_y@$ OCNT/NG possess a similar carbon structure with a high graphitization degree (Figure S9, Supporting Information).

The X-ray photoelectron spectroscopy (XPS) was further carried out to determine the surface chemical states of the LC- $\text{Ni}_x\text{Fe}_y@$ OCNT/NG and HC- $\text{Ni}_x\text{Fe}_y@$ OCNT/NG. As shown in Figure 1F, the high-resolution Ni $2p_{3/2}$ XPS spectra of LC- $\text{Ni}_x\text{Fe}_y@$ OCNT/NG are deconvoluted into three peaks at 852.9, 855.5, and 860.8 eV, respectively, representing the metallic Ni (Ni^0), oxidized Ni (Ni^{2+}), and satellite peak.^[20,29–31] Further, the high-resolution Fe $2p$ XPS spectra of LC- $\text{Ni}_x\text{Fe}_y@$ OCNT/NG exhibit three distinct Fe species including metallic Fe (Fe^0 , 707.8 and 721.4 eV), Fe^{2+} (711.3 and 724.2 eV), and Fe^{3+} (716.6 and 730.7 eV).^[31–34] Similar assignments are also observed for the HC- $\text{Ni}_x\text{Fe}_y@$ OCNT/NG. Consequently, the presence of metallic Ni and Fe peaks confirms the formation of Ni_xFe_y alloy, which is consistent with the above XRD and morphological analysis results. Meanwhile, the existence of oxidized species is attributed to the inevitable oxidation of the alloy surface layer.

The LC- $\text{Ni}_x\text{Fe}_y@$ OCNT/NG modified separator was prepared by coating the LC- $\text{Ni}_x\text{Fe}_y@$ OCNT/NG onto the commercial PP separator through a vacuum filtration process. The folding, bending, twisting, and tensile tests confirm the mechanical integrity of the modified separator and the strong adhesion between PP and LC- $\text{Ni}_x\text{Fe}_y@$ OCNT/NG (Figure S10, Supporting Information). The morphology difference between the pristine PP and LC- $\text{Ni}_x\text{Fe}_y@$ OCNT/NG modified separators is observed from the top-view SEM image (Figure 2A). The LC- $\text{Ni}_x\text{Fe}_y@$ OCNT/NG was uniformly coated onto the surface of PP separator with a coating thickness of $\approx 27 \mu\text{m}$, as confirmed by the distribution of each element onto the separator in the

cross-sectional SEM and EDX mapping images (Figure 2B–F). In sharp contrast to the pristine PP separator, the LC- $\text{Ni}_x\text{Fe}_y@$ OCNT/NG modified separator exhibits an excellent wettability to electrolyte solution (Figure 2G,H), which can facilitate the penetration of Li ions across the separator to achieve easy access to active sites. For comparison, the HC- $\text{Ni}_x\text{Fe}_y@$ OCNT/NG modified separator was prepared under the same condition (Figures S11–S13, Supporting Information).

In order to understand how the LC- $\text{Ni}_x\text{Fe}_y@$ OCNT/NG modified separator prevents the shuttling of LiPSs, in situ Raman spectroscopy was implemented to monitor a working LSB system. CR2032 coin cell was assembled using the as-modified separator, Li foil, and multiwalled carbon nanotube/sulfur (MWCNT/S) composites with 77 wt.% sulfur content (Figure S14, Supporting Information). The holes were tailored on the cell cap and Li foil to enable the laser access separator surface (Figure S15, Supporting Information), then the Raman signal was collected from the separator at the side near Li anode to accurately disclose the deposition of LiPSs on the separator. Figure 2I–L exhibit the time-resolved Raman spectra of LSBs with PP and LC- $\text{Ni}_x\text{Fe}_y@$ OCNT/NG separators during a discharge process at 0.2 C. Upon the initial discharging at ≈ 2.3 V, three Raman peaks of the PP separator appear at 146, 214, and 476 cm^{-1} corresponding to long-chain Li_2S_8 .^[35] The Raman characteristic peaks of Li_2S_8 gradually vanished at the second discharging of ≈ 2.1 V, while the strong peaks at 407, 451, and 510 cm^{-1} start to be emerged due to the formation of short-chain S_6^{2-} , S_5^{2-} , and $\text{S}_4^{2-}/\text{S}_3^{2-}$ until the end of discharge process (≈ 1.7 V).^[36,37] Similarly, the characteristic peaks of LiPSs can be also detected along with the whole charge process (Figure S16A,B Supporting Information). By contrast, very weak Raman signals of LiPSs are observed for the LC- $\text{Ni}_x\text{Fe}_y@$ OCNT/NG modified separator through the entire discharge and charge processes (Figure S16C,D Supporting Information), indicating the restrained LiPSs shuttling. The suppression of the shuttle effect was further confirmed using XPS (Figure S17, Supporting Information). Two peaks of 161.5 and 162.1 eV are assigned to the $2p_{3/2}$ and $2p_{1/2}$ spectra of long-chain Li_2S_x , respectively, while the peaks at 160.2 and 160.8 eV are ascribed to Li_2S signals.^[38] It notes that the observation of LiPSs on the lithium anode side confirms the shuttled movement of LiPSs from the cathode to the anode. Thus, no obvious intensities of peaks corresponding to Li_2S_x and Li_2S are observed for the LSB cell with LC- $\text{Ni}_x\text{Fe}_y@$ OCNT/NG separator, indicating that the LC- $\text{Ni}_x\text{Fe}_y@$ OCNT/NG contributes to suppressing the shuttle effect of LiPSs.

The effect of LC- $\text{Ni}_x\text{Fe}_y@$ OCNT/NG modified separator on Li^+ deposition was explored by testing the Li||Li symmetric cells at 0.5 mA cm^{-2} for >400 h with 1 h stripping–plating time. As shown in Figure 2M, the symmetric cells with the HC- $\text{Ni}_x\text{Fe}_y@$ OCNT/NG, OCNT/NG, and bare PP separators deliver large potential hysteresis of 21, 24, and 42 mV, respectively, showing unstable voltage fluctuation after long-term cycling. On the other hand, the cell with the LC- $\text{Ni}_x\text{Fe}_y@$ OCNT/NG modified separator achieves a small potential hysteresis of 9 mV with faint voltage fluctuation after 400 h cycling, implying the great potential for the homogeneous Li deposition.^[39–41] This Li plating–stripping behavior is attributed to an ionic sieving capability of the LC- $\text{Ni}_x\text{Fe}_y@$ OCNT/NG that can uniformly redistribute the Li^+ flux and effectively control the Li deposition.

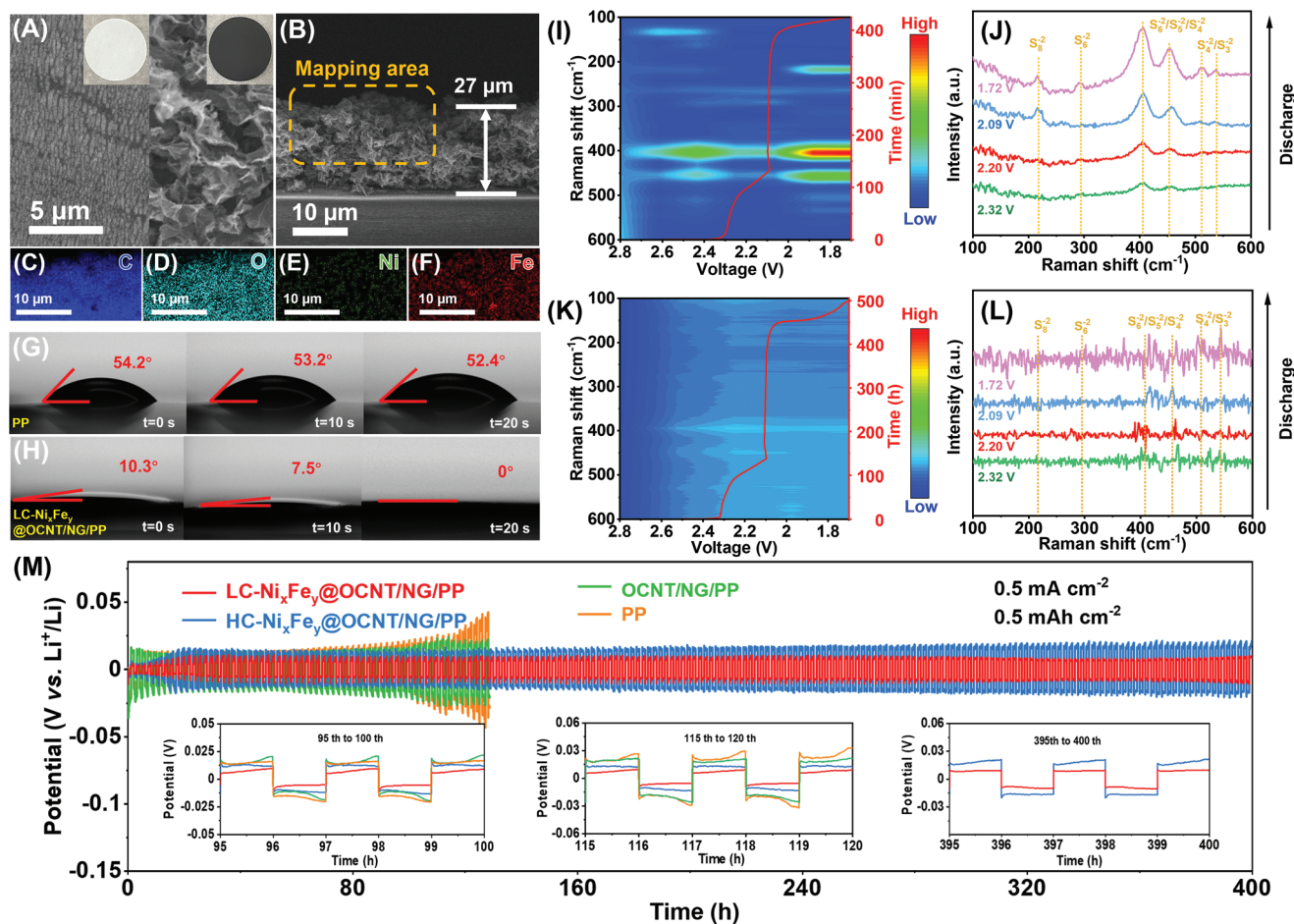


Figure 2. A) SEM images (including optical photographs) of PP (left) and LC-Ni_xFe_y@OCNT/NG/PP separators; B) cross-sectional SEM and C–F) EDS mapping images of LC-Ni_xFe_y@OCNT/NG/PP separator and SAED patterns; G, H) contact angle tests of PP (up) and LC-Ni_xFe_y@OCNT/NG/PP separators (down) under different time; I, J) In situ time-resolved Raman spectra achieved during the discharging processes with PP and LC-Ni_xFe_y@OCNT/NG/PP separators; K, L) selected Raman spectroscopy of LSB coin cells based on PP and LC-Ni_xFe_y@OCNT/NG/PP separators. The red plots represent the discharging processed; M) voltage curves of the lithium plating and stripping process during the first cycle at 0.5 mA cm⁻² with a constant capacity of 0.5 mAh cm⁻².

The electrochemical performances of LSBs with different separators were investigated using CR2032 coin cells. The separators for as-assembled cells were designated as LC-Ni_xFe_y@OCNT/NG/PP, HC-Ni_xFe_y@OCNT/NG/PP, OCNT/NG/PP, and PP, respectively. **Figure 3A** shows the cyclic voltammetry (CV) plots of the cells ranging the potential window from 1.7 to 2.8 V at a scan rate of 0.1 mV s⁻¹. Two distinct cathodic peaks, corresponding to the reduction of S₈ to long-chain soluble Li₂S_n (4 ≤ n ≤ 8) and the following reduction into short-chain insoluble Li₂S/Li₂S₂, are observed at 2.34 V (Peak I) and 2.03 V (Peak II), respectively. Meanwhile, two anodic peaks at 2.32 V (Peak III) and 2.40 V (Peak IV) are associated with the oxidation of Li₂S/Li₂S₂ to high-order Li₂S_n and the oxidation to S₈, respectively.^[42] Obviously, the cells with LC-Ni_xFe_y@OCNT/NG/PP achieve a higher onset potential, smaller potential gap, and larger current density than those with HC-Ni_xFe_y@OCNT/NG/PP, OCNT/NG/PP, and PP, indicating more facile and reversible conversion kinetics. Moreover, the clear and sharp redox peaks of the cells with LC-Ni_xFe_y@OCNT/NG/PP are preserved at high scan rates up to 0.5 mV s⁻¹ (Figure 3B) and after second

cycles (Figure S18, Supporting Information). The Li⁺ diffusion coefficients of the cells were derived from the corresponding CV curves (Figure S19, Supporting Information) using the Randles–Sevcik equation (see the Experimental Section for details).^[43] Particularly, the cells with LC-Ni_xFe_y@OCNT/NG/PP achieve the highest Li⁺ diffusion coefficients among other counterparts (Figure 3C; Figure S20 and Table S2, Supporting Information). Both fresh and cycled cells with LC-Ni_xFe_y@OCNT/NG/PP exhibit lower charge transfer resistances than those of the others (Figure 3D,E).^[44] These results confirm the contribution of fast Li⁺ transport and charge transfer kinetics by LC-Ni_xFe_y@OCNT/NG to the facilitated redox kinetics of sulfur conversion.

As shown in the galvanostatic charge/discharge (GCD) curves in Figure 3F, the initial discharge capacity of LSB cells with LC-Ni_xFe_y@OCNT/NG/PP is 1379.13 mAh g⁻¹ at 0.1 C, which is higher than those with HC-Ni_xFe_y@OCNT/NG/PP (1266.19 mAh g⁻¹), OCNT/NG/PP (1086.20 mAh g⁻¹), and PP (722.70 mAh g⁻¹), respectively. The polarization of LC-Ni_xFe_y@OCNT/NG/PP is 0.170 V, which is much smaller than those of

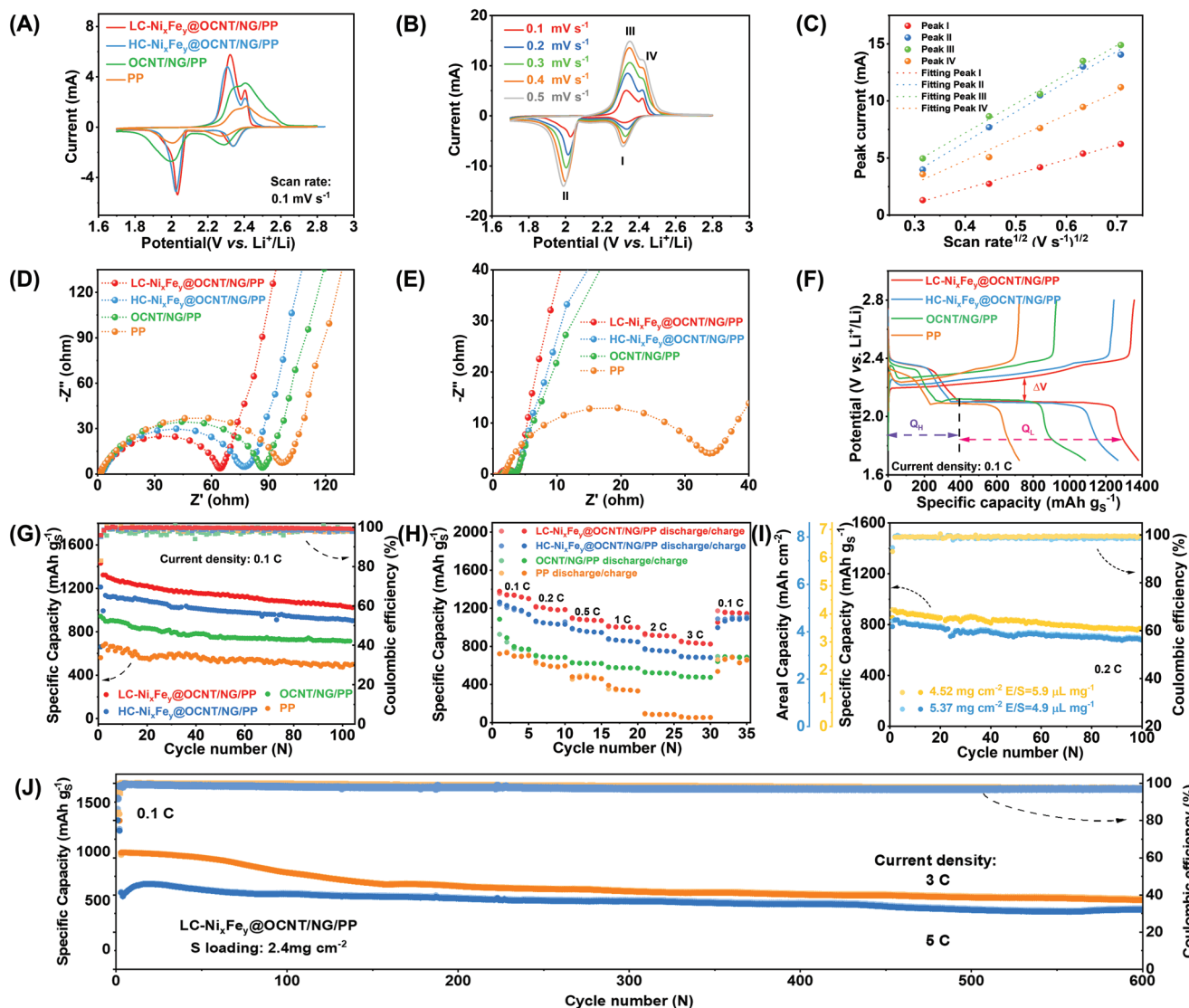


Figure 3. A) CV profiles of LSB coin cells based on different separators of PP, OCNT/NG/PP, HC-Ni_xFe_y@OCNT/NG/PP, and LC-Ni_xFe_y@OCNT/NG/PP separators; B) CV profiles LSB coin cells based on LC-Ni_xFe_y@OCNT/NG/PP separator at scan rates from 0.1 to 0.5 mV s⁻¹; C) plots of scan rate^{1/2} versus peak current of LSB coin cells with LC-Ni_xFe_y@OCNT/NG/PP separator; D,E) Nyquist plots of the LSB coin cells with different separators before and after cycling test; F,G) GCD curves and cycling performance of LSB coin cells with different separators at 0.1 C; H) the specific capacities of LSB coin cells with different separators at various C-rates; I) the cycling performance of LSB coin cells based on LC-Ni_xFe_y@OCNT/NG/PP separator with high sulfur loading amount at 0.2 C; J) long cycling performance of LSB coin cells with LC-Ni_xFe_y@OCNT/NG/PP separator at 3 C and 5 C rates.

HC-Ni_xFe_y@OCNT/NG/PP (0.205 V), OCNT/NG/PP (0.216 V), and PP (0.234 V), respectively, indicating the enhanced redox kinetics of sulfur conversion. The ratio of capacity contribution (denoted as Q_L/Q_H) from two discharge plateaus was estimated confirming the highest Q_L/Q_H value of LC-Ni_xFe_y@OCNT/NG/PP owing to the fast conversion kinetics (Table S3, Supporting Information).^[45] The specific and rate capacities of the LSBs with different separators were also measured (Figures S21 and S22, Supporting Information). As shown in Figure 3G, the specific capacities of LC-Ni_xFe_y@OCNT/NG/PP were 1379.13, 1218.29, 1189.99, 1099.85, 1013.44, 933.60, and 855.73 mAh g⁻¹ at the rates of 0.1, 0.2, 0.5, 1.0, 2.0, and 3.0 C, respectively, indicating the good rate capability. When the current rate is recovered to 0.1 C, the LSBs with LC-Ni_xFe_y@OCNT/NG/PP preserve

a high capacity of 1142.95 mAh g⁻¹ at fifth cycle. Particularly, the reversibility of LSB cells with LC-Ni_xFe_y@OCNT/NG/PP is confirmed as demonstrated by a high specific capacity of 1035.78 mAh g⁻¹ over 100 cycles (Figure 3H). On the other hand, the specific capacities of 912.19, 715.66, and 474.41 mAh g⁻¹ were achieved for the HC-Ni_xFe_y@OCNT/NG/PP, OCNT/NG/PP, and PP, respectively, after 100 cycles.

In order to verify the practical application of LC-Ni_xFe_y@OCNT/NG/PP, the electrochemical performances of LSBs are evaluated at high sulfur mass loading (4.52 and 5.37 mg cm⁻²) and lean electrolyte conditions. As shown in Figure 3I, the LSB cells with LC-Ni_xFe_y@OCNT/NG/PP after the activation of first cycle deliver high areal capacities of 4.5 and 4.1 mAh cm⁻² at 0.2 C with low electrolyte/sulfur (E/S) ratios of 5.9 and 4.9 μL mg⁻¹,

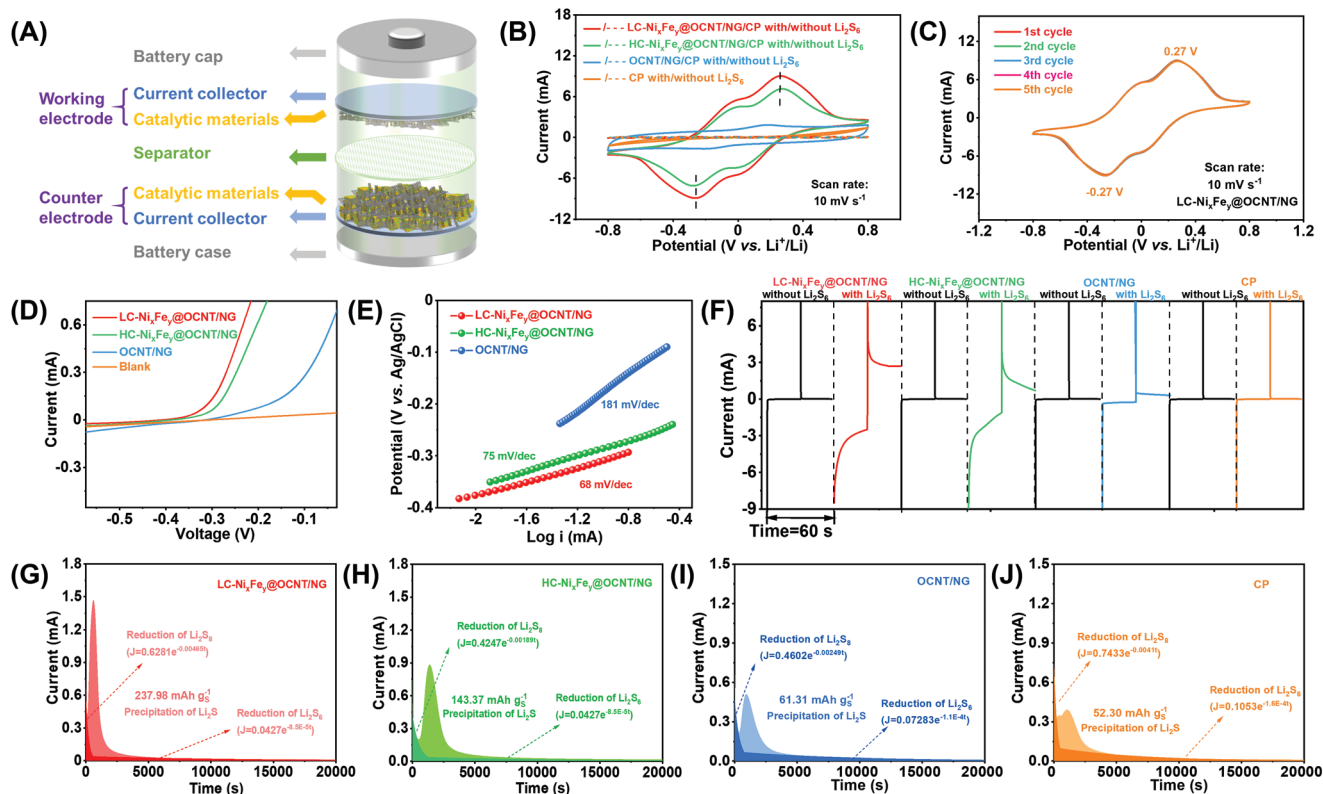


Figure 4. A) Schematic diagram of a symmetric cell; B) CV profiles of Li_2S_6 symmetric cells based on different identical electrodes; C) CV profiles of Li_2S_6 symmetric cells based on $\text{LC-Ni}_x\text{Fe}_y@OCNT/NG/CP$ electrodes with a scan rate of 10 mV s^{-1} ; D) LSV profiles and corresponding E) Tafel plots of sulfide oxidation reaction with different electrodes at 10 mV s^{-1} ; F) chronoamperometric curves of symmetric cells; G–J) potentiostatic discharge plots of different cells.

respectively. The areal capacities are retained at 3.7 and 3.5 mAh cm^{-2} after 100 cycles, which is higher than that of the LSB cell with $\text{HC-Ni}_x\text{Fe}_y@OCNT/NG/PP$ at 4.56 mg cm^{-2} with $5.7\text{ }\mu\text{L mg}^{-1}$ after 50 cycles (Figure S23, Supporting Information). Even at high current rates of 3 and 5 C, the LSB cells with $\text{LC-Ni}_x\text{Fe}_y@OCNT/NG/PP$ are stably operated for 600 cycles at the low fading rates of 0.08% per cycle and 0.04% per cycle, respectively, indicating long-term cyclic stability (Figure 3)). The cyclic performance of the LSB cells with $\text{LC-Ni}_x\text{Fe}_y@OCNT/NG/PP$ is superior to those of other metal alloy-based LSBs (Table S4, Supporting Information).

The inherent electrocatalytic activity of $\text{LC-Ni}_x\text{Fe}_y@OCNT/NG$ toward LiPS s conversion was verified using the symmetric cells. The $\text{LC-Ni}_x\text{Fe}_y@OCNT/NG$ loaded on carbon paper (CP) was used as both cathode and anode, while PP and $0.5\text{ M Li}_2\text{S}_6$ in dioxolane/dimethoxyethane (DOL/DME) (vol%: 1/1) served as separator and electrolyte, respectively (Figure 4A). As shown in Figure 4B, the $\text{LC-Ni}_x\text{Fe}_y@OCNT/NG/CP$ electrodes exhibit a higher current density and narrower peak separation in each redox pair than those of the $\text{HC-Ni}_x\text{Fe}_y@OCNT/NG/CP$ electrodes, promoting LiPS s conversion by the electrocatalytic activity. This electrocatalytic promotion was further verified demonstrating a small current response and no redox peaks in CV curve with $\text{LC-Ni}_x\text{Fe}_y@OCNT/NG/CP$ electrode in Li_2S_6 -free electrolytes. As shown in Figure 4C, the redox peaks of $\text{LC-Ni}_x\text{Fe}_y@OCNT/NG/CP$ electrode are preserved for five cycles better than those of the $\text{HC-Ni}_x\text{Fe}_y@OCNT/NG/CP$,

$OCNT/NG/CP$, and CP electrodes (Figure S24, Supporting Information), implying the superior electrocatalytic activity and electrochemical reversibility. Even at high scan rates, both distinct redox peaks and large current responses of $\text{LC-Ni}_x\text{Fe}_y@OCNT/NG/CP$ electrode are retained (Figure S25, Supporting Information).

Linear sweep voltammetry (LSV) curves are collected in a three-electrode system to investigate the effect of crystallinity regulation on the promoted kinetics of sulfur conversion.^[46] As shown in Figure 4D, the $\text{LC-Ni}_x\text{Fe}_y@OCNT/NG$ delivers a lower onset potential of -0.41 V compared to those of $\text{HC-Ni}_x\text{Fe}_y@OCNT/NG$ (-0.39 V) and $OCNT/NG$ (-0.32 V). Moreover, the $\text{LC-Ni}_x\text{Fe}_y@OCNT/NG$ contains a smaller Tafel slope of 68 mV dec^{-1} than those of $\text{HC-Ni}_x\text{Fe}_y@OCNT/NG$ (75 mV dec^{-1}) and $OCNT/NG$ (181 mV dec^{-1}) (Figure 4E). In comparison to the Li_2S_6 -free cells, the current response of Li_2S_6 symmetric cells is more prominent in chronoamperometry plots of $\text{LC-Ni}_x\text{Fe}_y@OCNT/NG$, $\text{HC-Ni}_x\text{Fe}_y@OCNT/NG$, and $OCNT/NG$ except for CP , which can exclude the contribution of double-layer capacitance (Figure 4F).^[47] Accordingly, the higher current response of $\text{LC-Ni}_x\text{Fe}_y@OCNT/NG$ than others indicates a larger electrocatalytic activity toward LiPS conversion in $0.5\text{ M Li}_2\text{S}_6$ in DOL/DME. These findings elucidate that the low crystallinity of NiFe alloy is attributed to high electrocatalytic activity and lowered energy barrier against LiPS conversion.

The Li_2S precipitation was further tested to demonstrate the effect of crystallinity regulation on the transformation of

LiPSs (Figure 4G–J). Impressively, the LC-Ni_xFe_y@OCNT/NG/CP electrode delivers a higher capacity of 237.98 mAh g⁻¹ for Li₂S precipitation compared with HC-Ni_xFe_y@OCNT/NG/CP (143.37 mAh g⁻¹), OCNT/NG/CP (61.31 mAh g⁻¹), and CP (52.30 mAh g⁻¹), respectively. Moreover, the LC-Ni_xFe_y@OCNT/NG/CP electrode also shows the shortest response time of Li₂S nucleation, implying that the LC-Ni_xFe_y@OCNT/NG with low crystallinity facilitates the Li₂S nucleation and LiPS conversion kinetics. Moreover, the dissolution of precipitated Li₂S was measured via a potentiostatic charging process (Figure S26, Supporting Information). The dissolution capacity of LC-Ni_xFe_y@OCNT/NG was much higher than those of HC-Ni_xFe_y@OCNT/NG, OCNT/NG, and CP, implying a more efficient oxidation process on the LC-Ni_xFe_y@OCNT/NG surface as verified by weak Li–S bonds in Li₂S. These results indicate the significant role of Ni_xFe_y alloy with low crystallinity on both nucleation and dissolution behavior of Li–S species.^[48]

In order to verify the adsorption capability of LC-Ni_xFe_y@OCNT/NG toward LiPSs, adsorption experiments were conducted (Figure S27, Supporting Information). After the 5 h soaking of LC-Ni_xFe_y@OCNT/NG, the color of the bottle filled with a 2.5 mmol L⁻¹ Li₂S₆ solution is changed from golden yellow into colorless. By contrast, the color of the bottle soaked with HC-Ni_xFe_y@OCNT/NG s becomes shallow yellow, while that of OCNT/NG exhibits no obvious change. Furthermore, the content of the residual Li₂S₆ in the supernatant solution was evaluated using UV–vis spectroscopy (Figure S27, Supporting Information). The distinctly reduced UV intensity for the LC-Ni_xFe_y@OCNT/NG is indicative of more effective adsorption of the LC-Ni_xFe_y than that of the HC-Ni_xFe_y alloy.

The enhanced adsorption capability of the LC-Ni_xFe_y alloy was further investigated by the first-principles calculation. The LC-Ni_xFe_y alloy structure was constructed by melting and quenching rapidly using ab initio molecular dynamic (AIMD). Compared with the HC-Ni_xFe_y alloy, the LC-Ni_xFe_y alloy exhibits obviously less atomic orderness (Figure S28, Supporting Information), indicating the successful preparation of the LC-Ni_xFe_y alloy structure. Based on the AIMD results, the model structures of LC-Ni_xFe_y and HC-Ni_xFe_y alloy anchored on NG surface were further established. Then, the absorption energies of LC-Ni_xFe_y/NG and HC-Ni_xFe_y/NG toward Li₂S, Li₂S₄ and Li₂S₆ were investigated as shown in Figure 5A, using DFT calculation. As shown in Figure 5B, all of the intermediates of Li₂S, Li₂S₄, and Li₂S₆ are more easily adsorbed on LC-Ni_xFe_y/NG surface, suggesting the more efficiently inhibited polysulfide shuttling of LC-Ni_xFe_y than HC-Ni_xFe_y alloy. The LC-Ni_xFe_y alloy features larger electron densities near Fermi level than that of the HC-Ni_xFe_y alloy (Figure 5C), implying that the formation of LiPSs and the redox kinetics could be facilitated on the LC-Ni_xFe_y alloy surface. Moreover, the theoretical diffusion barrier energies of Li₂S₆ on LC-Ni_xFe_y/NG and HC-Ni_xFe_y/NG surfaces were calculated. Figure 5D,E shows that the as-calculated diffusion barrier energy for LC-Ni_xFe_y/NG is only 986.22 meV, much lower than 1369.9 meV of HC-Ni_xFe_y/NG. These results demonstrate that the LC-Ni_xFe_y alloy enables the faster diffusion of LiPSs than HC-Ni_xFe_y, thus resulting in the facilitated redox reaction in the LSB system.^[26]

3. Conclusion

In summary, the low crystalline Ni_xFe_y alloy nanoparticles grown on a nanostructured OCNT/NG network were successfully synthesized and uniformly coated on PP surface as a sulfiphilicity-lithiophilicity bifunctional separator for LSB system. Compared with the HC-Ni_xFe_y@OCNT/NG, the redox kinetics of sulfur conversion and absorption capability to LiPSs were more significantly improved for the LC-Ni_xFe_y@OCNT/NG with low crystallinity, as verified by experiments and theoretical calculations. Benefitting from these characteristics, the LC-Ni_xFe_y@OCNT/NG/PP delivered a high specific capacity of 1379.13 mAh g⁻¹ at 0.1 C retaining a high capacity of 410 mAh g⁻¹ with a low decay ratio of 0.04%/cycle over 600 cycles at 5 C. Even under high sulfur loading (5.37 mg cm⁻²) and lean electrolyte (E/S = 4.9 μL mg⁻¹) conditions, the LSB cells with LC-Ni_xFe_y@OCNT/NG/PP delivered a high areal capacity of 4.1 mAh cm⁻² at 0.2 C. This work provides new insights into the correlation between crystallinity and electrochemical properties of bimetal alloys as well as into the rational design of functional separators for high-performance LSBs.

4. Experimental Section

Synthesis of OCNT/NG Dispersion: OCNT was synthesized by oxidizing the commercial multi-walled carbon nanotubes (CNT) in an O₃ dispersion solution. The OCNT powder was obtained via lyophilization. The nitrogen-doped graphene oxide (NG) was also synthesized (see Supporting Information Experimental Section). Then, 20 mg of OCNT and 20 mg of NG were mixed and ultrasonically dispersed in 20 mL of NMP solvent for 3 h to form OCNT/NG dispersion.

Synthesis of NiFe-LDH@OCNT/NG-1 and NiFe-LDH@OCNT/NG-2: 0.1 mmol of nickel (II) nitrate hexahydrate (Ni(NO₃)₂ · 6H₂O), 0.3 mmol of iron (III) nitrate nonahydrate (Fe(NO₃)₃ · 9H₂O), and 2 mmol of urea (CH₂N₂O) were added into 20 mL of DI-water to form yellowish-green solution. Meanwhile, 20 mL of OCNT/NG dispersion was poured into a beaker. Next, the above yellowish-green solution was mixed with the OCNT/NG dispersion by stirring for 40 min to obtain a uniform mixture. Subsequently, the mixture was poured into a Teflon line (50 mL) and heated at 120 °C for 6 h. After the reaction, the mixture was rinsed with DI-water for several times via centrifugation and freeze-dried to obtain the NiFe-LDH@OCNT/NG-1 powder. NiFe-LDH@OCNT/NG-2 was synthesized at the same conditions by adjusting the amount of Fe(NO₃)₃ · 9H₂O and Ni(NO₃)₂ · 6H₂O into 0.1 and 0.3 mmol, respectively.

Synthesis of LC-NixFey@OCNT/NG and HC-NixFey@OCNT/NG: The as-prepared NiFe-LDH@OCNT/NG-1 and NiFe-LDH@OCNT/NG-2 samples were put into the quartz boat and heated to 500 °C for 2 h in Ar gas atmosphere. After the reaction, the LC-Ni_xFe_y@OCNT/NG and HC-Ni_xFe_y@OCNT/NG samples were obtained.

Synthesis of LC-NixFey@OCNT/NG and HC-NixFey@OCNT/NG Modified PP Separator: 5 mg of LC-Ni_xFe_y@OCNT/NG powder was dispersed into 20 mL of NMP solvent by sonicating for 60 min. Then, 0.56 mg of polyvinylidene fluoride (PVDF) binder was added to the above dispersion and stirred for another 60 min. The as-prepared LC-Ni_xFe_y@OCNT/NG suspension was vacuum-filtered and covered on PP surface (Celgard 2400). Next, the LC-Ni_xFe_y@OCNT/NG modified PP separator was vacuum dried for 12 h at room temperature. Finally, LC-Ni_xFe_y@OCNT/NG/PP was cut into disks for the coin cell fabrication with a diameter of 19 mm and mass loading of ≈0.35 mg cm⁻². The HC-Ni_xFe_y@OCNT/NG modified PP separator was also prepared following the same process.

Computational Details: All DFT calculations were performed using Vienna Ab initio Simulation Package (VASP).^[49] Projector-augmented

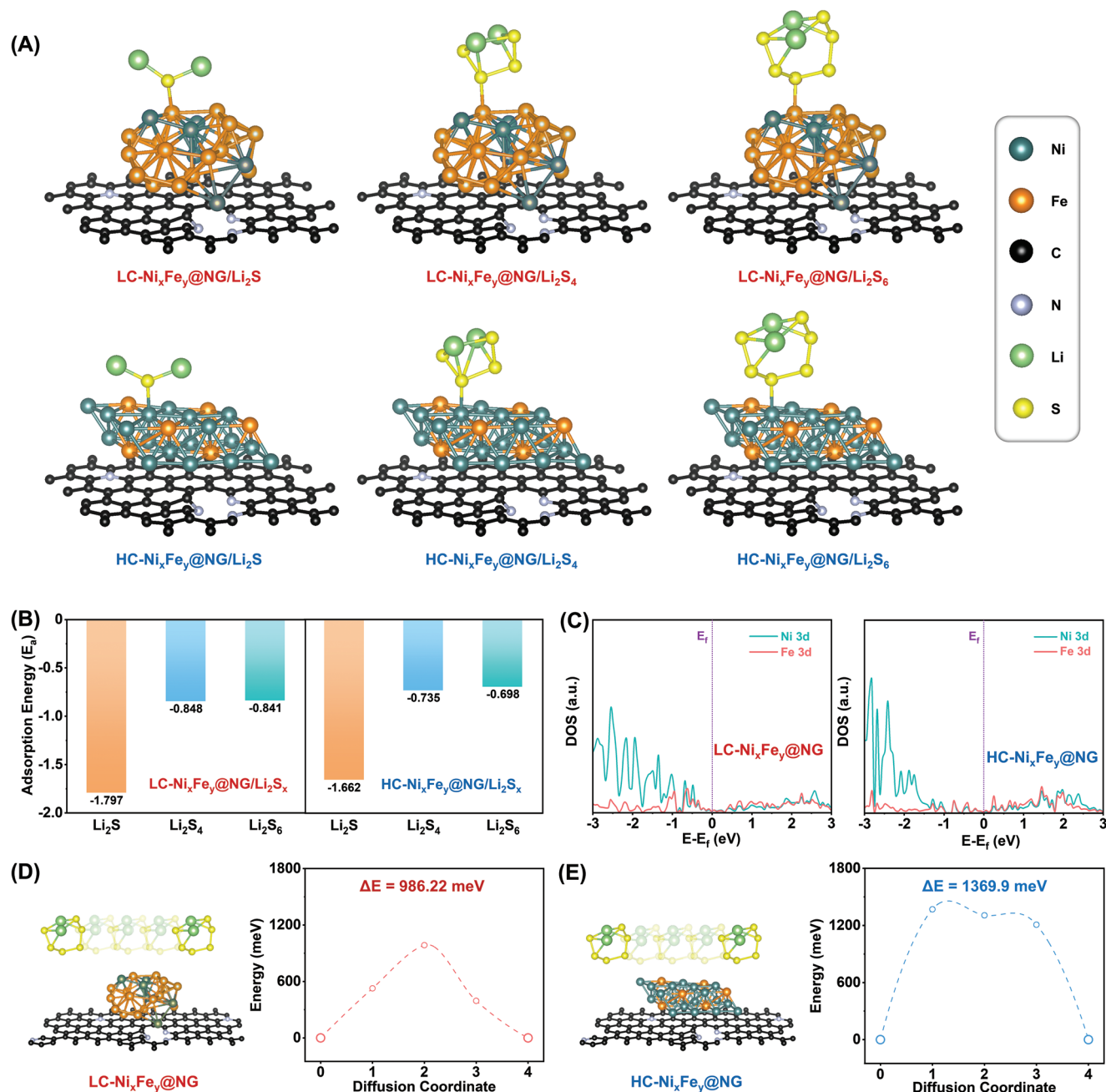


Figure 5. A) Li_2S , Li_2S_4 and Li_2S_6 -adsorbed LC- $\text{Ni}_x\text{Fe}_y/\text{NG}$ and HC- $\text{Ni}_x\text{Fe}_y/\text{NG}$ structures used for DFT calculation; B) The calculated adsorption energies of Li_2S , Li_2S_4 and Li_2S_6 at LC- $\text{Ni}_x\text{Fe}_y/\text{NG}$ and HC- $\text{Ni}_x\text{Fe}_y/\text{NG}$; C) The pDOSs of Ni 3d and Fe 3d of LC- $\text{Ni}_x\text{Fe}_y/\text{NG}$ and HC- $\text{Ni}_x\text{Fe}_y/\text{NG}$; D,E) The calculated diffusion energy barriers of Li_2S_6 on LC- $\text{Ni}_x\text{Fe}_y/\text{NG}$ and HC- $\text{Ni}_x\text{Fe}_y/\text{NG}$.

wave (PAW) pseudopotentials^[50] with a plane-wave basis set as implemented in VASP was used in this work. Perdew–Burke–Ernzerhof (PBE) parametrization of the generalized gradient approximation (GGA)^[51] was used for the exchange–correlation functional. For DFT calculations, a $2 \times 2 \times 2$ k-point grid was used to calculate the $\text{Ni}_x\text{Fe}_y/\text{NG}$ structure. For the more accurate calculation of van der Waals interaction between Li_2S_6 and substrate, the DFT-D3 correction method^[52] was considered in this study. The GGA+U method^[53] was adopted to address the localization of the d-orbital in Ni and Fe ions, with a U value of 5.5 and 3.0 eV, respectively.^[54] A kinetic energy cutoff of 400 eV was used in all the calculations, and all the structures

were optimized until the force in the unit cell converged to within $0.03 \text{ eV } \text{\AA}^{-1}$.

AIMD calculations were performed with the NVT ensemble, as implemented in VASP. During AIMD, the lattice parameters were fixed in a fully relaxed state of Ni_xFe_y structure within the GGA+U method. At first, we held the temperature at 3000 K to mimic the liquid state of Ni_xFe_y during 10 ps. The melted structure was quenched to room temperature (300 K) and then allowed to fully relax (within the GGA). The time step and quenching rates were 2 fs and 200 K ps^{-1} , respectively.

In this study, adsorption energy (E_{ads}) was calculated following the equation:

$$E_{\text{ads}} = E_{\text{surface@Li-S}} - (E_{\text{surface}} + E_{\text{Li-S}}) \quad (1)$$

where $E_{\text{surface@Li-S}}$ is the total energy of the substrate, which is adsorbed with lithium sulfide molecule, E_{surface} is total energy of the pristine substrate, and $E_{\text{Li-S}}$ is the total energy of lithium sulfide molecule, respectively.

Supporting Information

Supporting Information is available from the Wiley Online Library or from the author.

Acknowledgements

Q. L. and X. H. contributed equally to this work. This study was supported by a grant from the R&D Program of the Korea Railroad Research Institute (PK2203F1) and the National Research Foundation of Korea (NRF) grant funded by the Korea government (MSIT) (NRF2020M2D8A2070866), Republic of Korea.

Conflict of Interest

The authors declare no conflict of interest.

Data Availability Statement

The data that support the findings of this study are available from the corresponding author upon reasonable request.

Keywords

bimetallic alloys, crystallinity regulation, functional separators, lithium-sulfur batteries, redox kinetics

Received: June 21, 2022

Revised: August 12, 2022

Published online: September 28, 2022

- [1] M. Armand, J. Tarascon, *Nature* **2008**, 451, 652.
 [2] A. Manthiram, S. H. Chung, C. Zu, *Adv. Mater.* **2015**, 27, 1980.
 [3] Y. Yang, G. Zheng, Y. Cui, *Chem. Soc. Rev.* **2013**, 42, 3018.
 [4] M. Jana, R. Xu, X.-B. Cheng, J. S. Yeon, J. M. Park, J.-Q. Huang, Q. Zhang, H. S. Park, *Energy Environ. Sci.* **2020**, 13, 1049.
 [5] Z. Sun, J. Zhang, L. Yin, G. Hu, R. Fang, H.-M. Cheng, F. Li, *Nat. Commun.* **2017**, 8, 14627.
 [6] C. Wei, M. Tian, M. Wang, Z. Shi, L. Yu, S. Li, Z. Fan, R. Yang, J. Sun, *ACS Nano* **2020**, 14, 16073.
 [7] Y. Yan, P. Zhang, Z. Qu, M. Tong, S. Zhao, Z. Li, M. Liu, Z. Lin, *Nano Lett.* **2020**, 20, 7662.
 [8] S. Zhao, Y. Kang, M. Liu, B. Wen, Q. Fang, Y. Tang, S. He, X. Ma, M. Liu, Y. Yan, *J. Mater. Chem. A* **2021**, 9, 18927.
 [9] Y. Liu, Y. Yan, K. Li, Y. Yu, Q. Wang, M. Liu, *Chem. Commun.* **2019**, 55, 1084.
 [10] H. Ye, Y. Li, *Nano Res. Energy* **2022**, 1, e9129912.
 [11] Z. Wei, Y. Ren, J. Sokolowski, X. Zhu, G. Wu, *InfoMat.* **2020**, 2, 483.
 [12] J.-Q. Huang, Q. Zhang, F. Wei, *Energy Storage Mater.* **2015**, 1, 127.
 [13] Q. Liu, X. Han, H. Park, J. Kim, P. Xiong, H. Yuan, J. S. Yeon, Y. B. Kang, J. M. Park, Q. Dou, B.-K. Kim, H. S. Park, *ACS Appl. Mater. Interfaces* **2021**, 13, 17978.
 [14] H.-J. Peng, Z.-W. Zhang, J.-Q. Huang, G. Zhang, J. Xie, W.-T. Xu, J.-L. Shi, X. Chen, X.-B. Cheng, Q. Zhang, *Adv. Mater.* **2016**, 28, 9551.
 [15] J. Balach, T. Jaumann, M. Klose, S. Oswald, J. Eckert, L. Giebeler, *Adv. Funct. Mater.* **2015**, 25, 5285.
 [16] J. Zhu, Y. Ge, D. Kim, Y. Lu, C. Chen, M. Jiang, X. Zhang, *Nano Energy* **2016**, 20, 176.
 [17] S. Bai, X. Liu, K. Zhu, S. Wu, H. Zhou, *Nat. Energy* **2016**, 1, 16094.
 [18] Q. Liu, X. Han, Q. Dou, P. Xiong, Y. B. Kang, S. W. Kang, B.-K. Kim, H. S. Park, *Batteries & Supercaps* **2021**, 4, 1843.
 [19] H.-J. Peng, G. Zhang, X. Chen, Z.-W. Zhang, W.-T. Xu, J.-Q. Huang, Q. Zhang, *Angew. Chem., Int. Ed.* **2016**, 55, 12990.
 [20] J. He, A. Bhargava, A. Manthiram, *ACS Nano* **2021**, 15, 8583.
 [21] H. Li, L. Fei, R. Zhang, S. Yu, Y. Zhang, L. Shu, Y. Li, Y. Wang, *J. Energy Chem.* **2020**, 49, 339.
 [22] Y. Hu, C. Cheng, T. Yan, G. Liu, C. Yuan, Y. Yan, Z. Gu, P. Zeng, L. Zheng, J. Zhang, L. Zhang, *Chem. Eng. J.* **2021**, 421, 129997.
 [23] P. Zeng, C. Liu, X. Zhao, C. Yuan, Y. Chen, H. Lin, L. Zhang, *ACS Nano* **2020**, 14, 11558.
 [24] Z. Qiao, F. Zhou, Q. Zhang, F. Pei, H. Zheng, W. Xu, P. Liu, Y. Ma, Q. Xie, L. Wang, X. Fang, D.-L. Peng, *Energy Storage Materials* **2019**, 23, 62.
 [25] Z. Gu, C. Cheng, T. Yan, G. Liu, J. Jiang, J. Mao, K. Dai, J. Li, J. Wu, L. Zhang, *Nano Energy* **2021**, 86, 106111.
 [26] H. Yu, P. Xiao, P. Wang, Y. Yu, *Appl. Catal. B: Environ.* **2016**, 193, 217.
 [27] H. Han, H. Choi, S. Mhin, Y.-R. Hong, K. M. Kim, J. Kwon, G. Ali, K. Y. Chung, M. Je, H. N. Umh, D.-H. Lim, K. Davey, S.-Z. Qiao, U. Paik, T. Song, *Energy Environ. Sci.* **2019**, 12, 2443.
 [28] R. Sun, Y. Bai, M. Luo, M. Qu, Z. Wang, W. Sun, K. Sun, *ACS Nano* **2021**, 15, 739.
 [29] Q. Liu, X. Han, Q. Dou, P. Xiong, Y. Kang, B.-K. Kim, H. S. Park, *Int. J. Energy Res.* **2022**, 46, 9634.
 [30] C. Wang, H. Yang, Y. Zhang, Q. Wang, *Angew. Chem., Int. Ed.* **2019**, 58, 6099.
 [31] S. Payandeh, F. Strauss, A. Mazilin, A. Kondrakov, T. Brezesinski, *Nano Res. Energy* **2022**, 1, e9120016.
 [32] X. Han, C. Yu, J. Yang, X. Song, C. Zhao, S. Li, Y. Zhang, H. Huang, Z. Liu, H. Huang, X. Tan, J. Qiu, *Small* **2019**, 15, 1901015.
 [33] X. T. Han, C. Yu, Y. Y. Niu, Z. Wang, Y. B. Kang, Y. W. Ren, H. Wang, H. S. Park, J. S. Qiu, *Small Methods* **2020**, 4, 2000546.
 [34] L. Meng, L. Li, *Nano Res. Energy* **2022**, 1, e9120020.
 [35] M. Hagen, P. Schiffels, M. Hammer, S. Dörfler, J. Tübke, M. J. Hoffmann, H. Althues, S. Kaskel, *J. Electrochem. Soc.* **2013**, 160, A1205.
 [36] J. J. Chen, R. M. Yuan, J. M. Feng, Q. Zhang, J. X. Huang, G. Fu, M. S. Zheng, B. Ren, F. Q. Dong, *Chem. Mater.* **2015**, 27, 2048.
 [37] L. Zhang, Y. Liu, Z. Zhao, P. Jiang, T. Zhang, M. Li, S. Pan, T. Tang, T. Wu, P. Liu, Y. Hou, H. Lu, *ACS Nano* **2020**, 14, 8495.
 [38] R. Gao, Q. Zhang, Y. Zhao, Z. Han, C. Sun, J. Sheng, X. Zhong, B. Chen, C. Li, S. Ni, Z. Piao, B. Li, G. Zhou, *Adv. Funct. Mater.* **2022**, 32, 2110313.
 [39] Y. Yao, H. Wang, H. Yang, S. Zeng, R. Xu, F. Liu, P. Shi, Y. Feng, K. Wang, W. Yang, X. Wu, W. Luo, Y. Yu, *Adv. Mater.* **2020**, 32, 1905658.
 [40] H. Xue, H. Gong, Y. Yamauchi, T. Sasaki, R. Ma, *Nano Res. Energy* **2022**, 1, e9120007.
 [41] J. Liang, Q. Liu, A. A. Alshehri, X. Sun, *Nano Res. Energy* **2022**, e9120010.
 [42] Z. Yuan, H. J. Peng, T. Z. Hou, J. Q. Huang, C. M. Chen, D. W. Wang, X. B. Cheng, F. Wei, Q. Zhang, *Nano Lett.* **2016**, 16, 519.
 [43] Y.-S. Lee, K.-S. Ryu, *Sci. Rep.* **2017**, 7, 16617.
 [44] H. Kim, J. Lee, H. Ahn, O. Kim, M. J. Park, *Nat. Commun.* **2015**, 6, 7278.

- [45] C. Zhang, J. J. Biendicho, T. Zhang, R. Du, J. Li, X. Yang, J. Arbiol, Y. Zhou, J. Morante, R. A. Cabot, *Adv. Funct. Mater.* **2019**, *29*, 1908342.
- [46] D. Luo, Z. Zhang, G. Li, S. Cheng, S. Li, J. Li, R. Gao, M. Li, S. Sy, Y.-P. Deng, Y. Jiang, Y. Zhu, H. Dou, Y. Hu, A. Yu, Z. Chen, *ACS Nano* **2020**, *14*, 4849.
- [47] X. J. Hong, C. L. Song, Y. Yang, H. C. Tan, G. H. Li, Y. P. Cai, H. Wang, *ACS Nano* **2019**, *13*, 1923.
- [48] Z. Han, S. Zhao, J. Xiao, X. Zhong, J. Sheng, W. Lv, Q. Zhang, G. Zhou, H.-M. Cheng, *Adv. Mater.* **2021**, *33*, 2105947.
- [49] G. Kresse, J. Furthmüller, *Comput. Mater. Sci.* **1996**, *6*, 15.
- [50] P. E. Blöchl, *Phys. Rev. B.* **1994**, *50*, 17953.
- [51] J. P. Perdew, K. Burke, M. Ernzerhof, *Phys. Rev. Lett.* **1996**, *77*, 3865.
- [52] S. Grimme, J. Antony, S. Ehrlich, H. Krieg, *J. Chem. Phys.* **2010**, *132*, 154104.
- [53] V. I. Anisimov, F. Aryasetiawan, A. I. Lichtenstein, *J. Phys. Condens. Matter.* **1997**, *9*, 767.
- [54] J. Jiang, F. Sun, S. Zhou, W. Hu, H. Zhang, J. Dong, Z. Jiang, J. Zhao, J. Li, W. Yan, M. Wang, *Nat. Commun.* **2018**, *9*, 2885.